Chemical Geology 453 (2017) 72–79

Contents lists available at ScienceDirect

Chemical Geology

journal homepage: www.elsevier.com/locate/chemgeo

Immobilization of nanoparticles by occlusion into microbial calcite

Rebecca L. Skuce [a], Dominique J. Tobler [a,b], Ian MacLaren [c], Martin R. Lee [a], Vernon R. Phoenix [d,*]

[a] School of Geographical & Earth Sciences, Gregory Building, University of Glasgow, G12 8QQ, UK
[b] Nano-Science Center, Department of Chemistry, University of Copenhagen, Universitetsparken 5, 2100 Copenhagen Ø, Denmark
[c] School of Physics and Astronomy, University of Glasgow, G12 8QQ, UK
[d] Department of Civil and Environmental Engineering, University of Strathclyde, Glasgow, G1 1XJ, UK

ARTICLE INFO

Article history:
Received 6 December 2016
Received in revised form 3 February 2017
Accepted 4 February 2017
Available online 6 February 2017

Keywords:
Calcite
Occlusion
Nanoparticle
Bacteria
Ureolysis
Biomineralization

ABSTRACT

Binding of nanoparticles (NPs) to mineral surfaces influences their transport through the environment. The potential, however, for growing minerals to immobilize NPs via occlusion (the process of trapping particles inside the growing mineral) has yet to be explored in environmentally relevant systems. In this study, the ureolytic bacteria *Sporosarcina pasteurii* was used to induce calcium carbonate precipitation in the presence of organo-metallic manufactured nanoparticles. As calcite crystals grew the nanoparticles in the solution became trapped inside these crystals. Capture of NPs within the calcite via occlusion was verified by transmission electron microscopy of thin foils. Nanoparticles with a negative surface charge were captured with greater efficiency than those with a positive surface charge, resulting from stronger attachment of negative nanoparticles to the positively charged calcite surfaces, which in turn facilitated occlusion. Thermodynamic and kinetic analysis, however, did not reveal a significant difference in k_p (calcite precipitation rate constant) or the critical saturation at which precipitation initiates (S_{crit}), indicating the presence of different charged nanoparticles did not influence calcite precipitation at the concentrations used here. Overall, these findings demonstrate that microbially driven mineral precipitation has potential to immobilize nanoparticles in the environment via occlusion.

1. Introduction

Microorganisms have the ability to drive the precipitation of a wide range of minerals. This process can lead to the immobilization of dissolved metals, either within the crystalline structure of the mineral or bound to the mineral surface. For example, microbial oxidation of Fe(II) and Mn(II) generates metal (hydr)oxides which can absorb various dissolved heavy metals and metalloids (Martinez et al., 2004; Pei et al., 2013), while enzymatic precipitation of phosphate produces hydroxyapatite which binds significant quantities of dissolved heavy metals (Handley-Sidhu et al., 2011). Calcite precipitation is common in ground and surface water systems and can be abiotically or biotically driven. A variety of microbial pathways can drive calcite precipitation, including photosynthesis (Merz, 1992), denitrification (van Paassen et al., 2010) and sulphate reduction (Braissant et al., 2007). The capacity to hydrolyse urea (ureolysis) is common in soil and aquifer microorganisms and also has the ability to drive calcite precipitation (Fujita et al., 2010). This process can be manipulated for solid phase capture of heavy metals and radionuclides, where the foreign ion gets incorporated into the calcium carbonate crystal structure as it forms (e.g., ^{90}Sr replacing Ca in the crystal lattice), thus preventing their mobility in the subsurface (Warren et al., 2001). During ureolysis-driven calcium carbonate precipitation, urea is hydrolysed by the microbial enzyme urease, producing ammonia and carbonic acid (Eq. (1)), which then equilibrates in water to form bicarbonate, ammonium and hydroxide ions. This leads to a pH rise and if soluble calcium is present, an increase in $CaCO_3$ saturation state. Once $CaCO_3$ becomes supersaturated, $CaCO_3$ minerals such as calcite precipitate (Tobler et al., 2011) (Eq. (2)).

$$CO(NH_2)_2 + 2H_2O \leftrightarrows 2NH_3 + H_2CO_3 \quad (1)$$

$$Ca^{2+} + HCO_3^- \leftrightarrows CaCO_3 + H^+ \quad (2)$$

While solid phase capture of dissolved metals during microbial mineral precipitation is a well-known and studied process, the fate of nanometre sized particles during microbial mineral precipitation has not been examined in detail. With a rising demand for nanomaterials and continual growth in production, increased environmental exposure to manufactured nanoparticles (NPs) is likely (Caballero-Guzman and Nowack, 2016). NPs also occur naturally, and both manufactured and natural NPs can act as carriers of heavy metals and organic contaminants (Hofmann and von der Kammer, 2009). To date, investigations into the impact of minerals on nanoparticle transport and fate in the natural environment have largely focused upon the adhesion of

* Corresponding author.
E-mail address: vernon.phoenix@strath.ac.uk (V.R. Phoenix).

http://dx.doi.org/10.1016/j.chemgeo.2017.02.005

nanoparticles to mineral surfaces (Basnet et al., 2015; Dietrich et al., 2012; Feriancikova and Xu, 2012). However, nanoparticles also have the potential to be immobilized by occlusion (the incorporation of a nanoparticle inside the growing mineral). Thus far however, exploration of how nanoparticles are occluded into minerals has largely been the focus of advanced materials research, where nanoparticles are incorporated to generate synthetic mineral composites with unique properties (Cho et al., 2016; Kim et al., 2010; Kim et al., 2016). As it stands, there is a dearth of information on how occlusion process may impact nanoparticle availability in natural settings. To explore this further, we here utilize a simple, controllable model system – calcite precipitation driven by bacteria. This is relevant as microbial calcite precipitation can occur naturally, but can also be accelerated by stimulation of microbial communities for the purpose of trapping pollutants (Fujita et al., 2010; Mitchell and Ferris, 2005).

In this study, calcite precipitation was driven by the ureolytic bacterium *Sporosarcina pasteurii* (*S. pasteurii*). Experiments were performed as a function of NP surface charge and size to determine if these factors impacted capture efficiency. Capture efficiency was determined by analysing the amount of NPs removed from solution, with capture confirmed by transmission electron microscopy of calcite sections. Thermodynamic and kinetic interpretation of results were undertaken to determine whether these NP properties had a significant impact on precipitation kinetics and the saturation state required for precipitation.

2. Materials and methods

2.1. Nanoparticles

The NPs used in this study exhibit exceptionally high stability, even under high ionic strength, and thus do not aggregate in solution. This is important here as this study aims to demonstrate that NPs can be removed from suspension by occlusion as opposed to aggregation processes. Three different types of NPs were obtained from BioPAL, USA: large negatively charged NP (FeREX, Ø = 150 nm, −38 mV), small negatively charged NP (Molday ION carboxyl terminated, Ø = 35 nm, −38 mV) and small positively charged NPs (Molday ION C6Amine, Ø = 35 nm, +48 mV), They all have a 10 nm nanomagnetite (Fe_3O_4) core surrounded by dextran. Different size and surface charge result from differing thickness of dextran and differing functional groups upon the dextran. This allowed testing the effect of surface charge and particle size on the NP removal efficiency.

Because all NPs types contained identical nanomagnetite cores, Fe was used as a proxy for NP concentration. This enabled NP concentrations to be determined by acid digestion followed by Fe analysis by atomic adsorption spectroscopy (AAS). The initial NP concentration for each experiment was 10 mg L^{-1} Fe. This corresponded to approximately 10^{16} nanoparticles per litre.

2.2. Experimental design

Batch experiments were performed using the gram positive, ureolytic bacterium *S. pasteurii* (strain ATCC 11859). Cultures were grown at 25 °C in brain heart infusion supplemented with filter-sterilised urea (20 g L^{-1}). Cells in exponential phase growth were harvested by vacuum filtration (using sterile 0.2 μm membrane filters) and rinsed twice with sterile deionised water (SDW). The bacterial pellet was re-suspended in SDW to an optical density (OD) of 0.14 as determined spectrophotometrically at 600 nm and then pH adjusted to 6.5 using HCl (Analar grade). An OD of 0.14 equates to 2.3×10^6 cells mL^{-1}, based on the *S. pasteurii* OD to cell conversion in (Levard et al., 2012). For each nanoparticle immobilization experiment (here-in referred to as NP-I experiment), a solution containing 100 mM $CaCl_2$ and 100 mM urea was prepared and then mixed at a ratio of 1:1 with the bacterial suspension followed by the immediate addition of nanoparticles. The final concentrations were 50 mM $CaCl_2$, 50 mM urea, 10 mg L^{-1} nanoparticles (Fe concentration) and 0.07 OD *S. pasteurii*. During the experiment these batch incubations remained static (i.e. not stirred). In one experiment with l-negNPs, a second injection of 50 mM urea and $CaCl_2$ solution was added into the batch reaction once all initially added urea was converted (using 1 M stock solutions to minimise dilution), to determine if any non-captured NPs could be trapped by a second phase of calcium carbonate precipitation. All nanoparticle immobilization experiments were carried out in triplicate in glass beakers that were covered with *parafilm* to prevent evaporation. Biotic (*S. pasteurii* + urea + NP) and abiotic ($CaCl_2$ + urea + NP) control experiments were also run. In these control experiments, the absence of either bacteria or $CaCl_2$ prevented microbial calcite precipitation, thus revealing if NPs were removed via other mechanisms.

2.3. Chemical analysis

Analyses of solution pH and dissolved NH_4, Ca and Fe were determined at time zero and at regular time intervals thereafter. At each sampling time, 10 mL aliquots were removed from the experiment; 5 mL were used for pH measurement, 0.5 mL to determine NH_4^+ by the Nessler assay and 4.5 mL were mixed with 0.5 mL concentrated HCl for Ca and Fe analyses using atomic absorption spectrometry (AAS, Thermo Scientific iCE 3000 Series). The error for Ca and Fe AAS measurements as determined from repeated measurements of the same sample was within analytical uncertainty (≤5%).

2.4. Transmission electron microscopy (TEM)

TEM imaging, selected area electron diffraction (SAED) and energy-dispersive X-ray spectroscopy (EDXS) were undertaken on thin foils that were prepared from calcite grains using the Focused Ion Beam (FIB) lift-out technique with a FEI Nova 200 Dualbeam. Calcite crystal surfaces were first sputter coated with gold to prevent charging of the mineral surface and ion-implantation into the calcite, followed by further deposition of platinum from an organometallic precursor within the FIB. Foils were thinned using a 30 kV Ga^+ ion beam to a thickness of ~1 μm prior to being removed from their parent grain using an in-situ micromanipulator. Foils were welded to the tines of an Omniprobe copper support using electron and ion beam deposited platinum. Final thinning was performed using lower accelerating voltages and beam currents on these supported thin foils to reduce the total thickness to less than ~60 nm in the thinnest areas in order to facilitate EELS (Electron Energy Loss Spectroscopy), without compromising the crystallinity. Initial characterisation of these foils by diffraction-contrast imaging and SAED was performed using a FEI T20 TEM operated at 200 kV. EELS analysis was performed using a JEOL ARM200F equipped with a Gatan GIF Quantum Electron Energy Loss Spectrometer; the EELS work was undertaken at an accelerating voltage of 80 kV in scanning TEM (STEM) mode using line scans with a nominal step size of about 1 nm.

2.5. Kinetic analysis of calcite precipitation

To determine if the presence of NPs and their properties (size and surface charge) affected $CaCO_3$ precipitation rates (e.g., through NPs acting as nucleation sites and/or growth inhibitors), we determined calcite precipitation kinetics as described in Tobler et al. (2011). See supplemental information for details of calculations. In summary, the rate constant for calcite precipitation (k_p) and the critical saturation at which precipitation initiates (S_{crit}), can be determined from the following first order reaction (Tobler et al., 2011).

$$\left[Ca^{2+}\right] = \left(\frac{k_p}{k_s}\right)\left[S - S_{crit} - \ln\left(\frac{S}{S_{crit}}\right)\right] + \left[Ca^{2+}\right]_{crit} \quad (3)$$

where $[Ca^{2+}]_{crit}$ is the dissolved Ca concentration at S_{crit} and k_s is a first

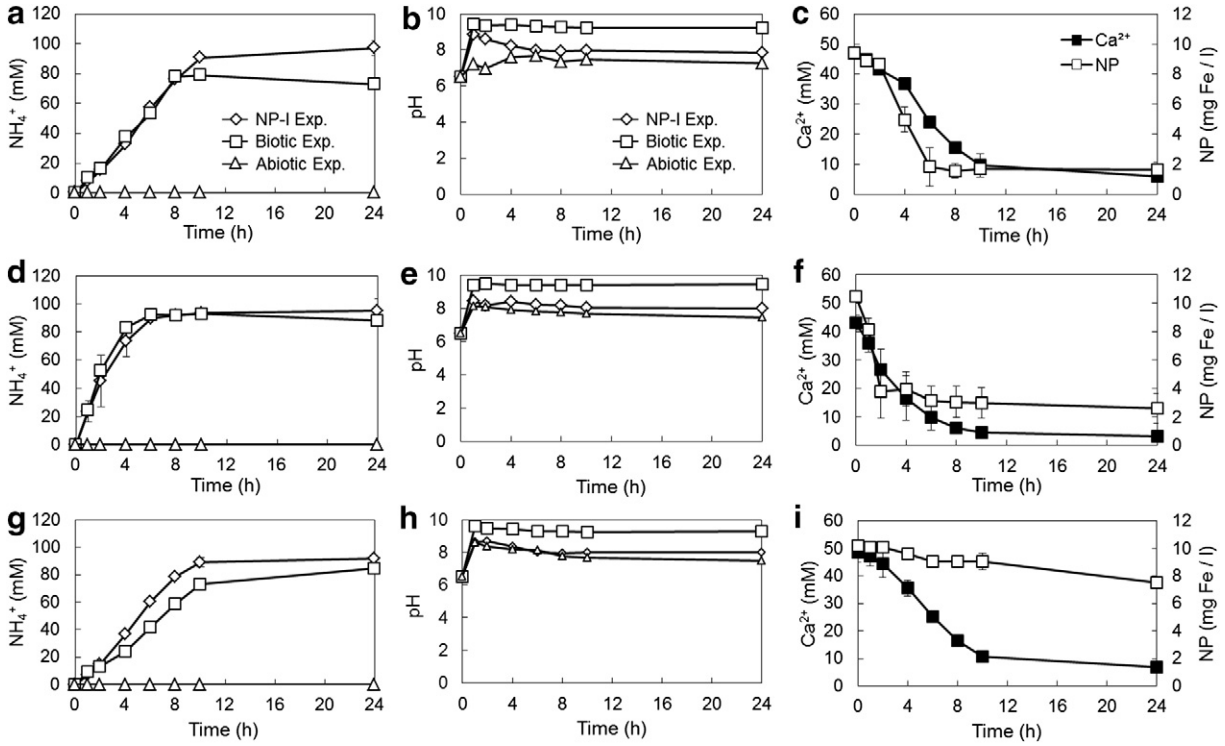

Fig. 1. Time series showing changes in NH_4^+ (a, d, g), pH (b, e, h) and dissolved Ca^{2+} and NP concentration (c, f, i) for the s-negNP (a, b, c), l-negNP (d, e, f) and s-posNP (g, h, i) experiments. NP-I Exp = nanoparticle immobilization experiment; Biotic Exp = biotic control experiment; Abiotic Exp = abiotic control experiment. Figures (c, f, i) show nanoparticle immobilization experiment only.

order rate constant. To estimate S_{crit} and k_p, Eq. (3) was fitted to the experimental data (i.e., S and $[Ca^{2+}]$ over time) using unconstrained non-linear regression and a quasi-Newton optimization routine for parameter estimation in the STATISTICA v.6.0 software package (Ferris et al., 2004).

2.6. DLVO calculations

To probe potential interactive forces between NPs and calcite, classical and extended Derjaguin-Landau-Verwey-Overbeek (DLVO and XDLVO) calculations were performed (Hoek and Agarwal, 2006; Hong et al., 2009). In the classical DLVO calculation, the total interaction energies (U_{DLVO}) between the calcite and nanoparticle surfaces can be described as the sum of the van der Waals (U_{vdW}) and electrostatic double layer (U_{elec}) forces:

$$U_{DLVO} = U_{vdW} + U_{elec} \quad (4)$$

These calculations can be extended to take into account the forces generated by the Lewis acid-base properties (U_{AB}) of the two surface:

$$U_{XDLVO} = U_{vdW} + U_{elec} + U_{AB} \quad (5)$$

In this model, we assume the NP is a sphere of dextran (ignoring the iron oxide core) because the surface interactions will occur between calcite and the thick dextran outer layer of the NP. Details of DLVO calculations are provided in supplemental information.

3. 3. Results and discussion

3.1. Immobilization of NPs

Immobilization of NPs was first tested on the small, negatively charged NPs (s-negNPs). In the nanoparticle immobilization experiment (NP-I), all urea was hydrolysed within 10 h (Fig. 1a), which was accompanied by a sharp rise in pH (Fig. 1b). Concomitantly, the dissolved Ca^{2+} rapidly decreased (Fig. 1c), showing that as urea is hydrolysed, the solution became rapidly supersaturated with respect to calcium carbonate, resulting in immediate $CaCO_3$ precipitation. Similarly, as calcium carbonate precipitated, the NP concentration in solution also decreased (Fig. 1c). Importantly, once Ca^{2+} removal ceased after 10 h, no further decrease in NP concentration was observed.

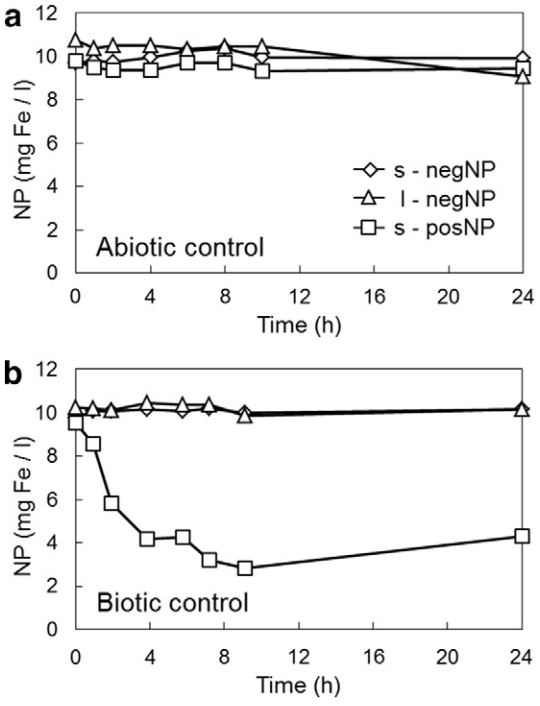

Fig. 2. Time series showing changes in Fe (NP) concentration for the (a) abiotic and (b) biotic control for all NP types tested.

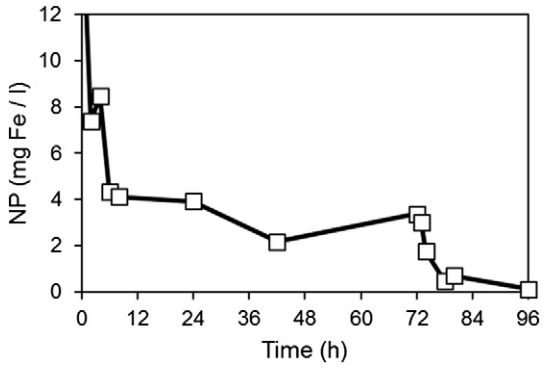

Fig. 3. Time series showing NP concentration during the double dose experiment for the l-negNP. The second dose of $CaCl_2$ and urea was injected at 72 h.

Overall, 83% of the s-negNPs were removed by $CaCO_3$ precipitation, with the majority of this occurring within only 6 h. Very similar trends for ureolysis, pH, Ca^{2+} and NP concentration (Fig. 1d, e, f) were observed for the larger, negatively charged NP (l-negNP). Again, substantial calcite precipitation occurred and significant quantities of l-negNPs were removed from solution in the NP-I experiment (Fig. 1f), although about 8% less l-negNPs were removed compared to in the s-negNP experiment.

The same set of experiments was conducted with small positive NPs (s-posNPs) to explore the impact of surface charge on capture efficiency. For the s-posNPs nanoparticle capture experiments, rates of urea hydrolysis, pH increase and removal of dissolved Ca^{2+} (Fig. 1g, h, i) were almost identical to those observed for the s-negNP experiment (Fig. 1, a, b, c). However, NP removal was substantially lower, with only 26% of the s-posNPs removed (Fig. 1i) compared to the removal of 83% of the s-negNPs. This highlights the importance of surface charge on capture efficiency.

NP removal did not occur in any of the abiotic controls (NP + $CaCl_2$ + urea) (Fig. 2a), confirming that both positively and negatively charged NPs were not removed by, for example, aggregation and settling, or attachment to reaction vessel walls. In the biotic controls (*S. pasteurii* + NP + urea), rates of ureolysis were basically identical to rates observed in NP-I experiments for the three NP types (Fig. 1a, d, g). Biotic controls also indicated whether any immobilization occurred through sorption onto bacterial cells. Immobilization by sorption to bacteria did not occur for the negatively charged NPs; NP levels remained constant at the initial concentration (Fig. 2b). However, in the biotic control of the s-posNP experiment, rapid loss of NPs occurred leading to a capture of over 60% within 12 h (Fig. 2b). This may not be surprising as the cell surface of *S. pasteurii* (and most other bacteria) is negatively charged over the pH range studied here (Yee et al., 2004), which evidently led to a strong electrostatic attraction between the bacterial cells and the positively charged nanoparticles. As the bacteria settled from solution they concomitantly removed s-posNPs from suspension. This process highlights the potential of bacterial surfaces to immobilize NPs in the natural environment and, for example, in engineered wastewater treatment systems as observed previously (Brar et al., 2010; Limbach et al., 2008). This raises the question whether s-posNPs also attached to cells in the NP-I experiments where calcite precipitation occurred, which could contribute to the removal of s-posNPs. The lower capture efficiency in the NP-I experiment compared to the biotic control might be explained by the presence of dissolved Ca^{2+} in the NP-I experiment, which could have reduced the surface charge of the bacterial cell.

Although there was good capture of negatively charged NPs, a small % were left in suspension at the end of the experiment (Fig. 1c & f). A short test was performed at the end of the l-negNP experiment to see if these remaining NPs could be removed during a second phase of calcite precipitation. Fig. 3 shows that with a second injection of $CaCl_2$ and urea (yielding final concentrations of 50 mM each), further calcium carbonate precipitation occurred resulting in capture of the remaining suspended NPs.

3.2. Imaging NP capture

The $CaCO_3$ precipitates that formed in the NP-I experiments were captured on glass slides placed at the bottom of the reaction vessels. Brown precipitates formed in NP-I experiments with negatively charged NPs due to the incorporation of brown coloured NPs (Fig. 4a) and in contrast, calcite precipitated by the same method but in the absence of NPs produced a near-white precipitate (Fig. 4b).

SEM analyses showed that calcite was the dominant mineral phase in all experiments, easily identified by the rhombohedral crystal morphology (Fig. 5a). It further showed the close association of bacterial cells with the calcite. In places the cells appear to be growing out of holes in the calcite. This is in fact bacteria being buried by calcite as the crystals grow. The presence of bacteria seemed to have led to more rounded crystal edges, although the overall rhombohedral shape was not affected. TEM images of thin foils cut from single crystals of calcite confirmed that the NPs occurred as occlusions within the calcite (i.e. they were trapped inside the crystal), (Fig. 5b). The crystal lattice is distorted around them producing butterfly-shaped strain contrast in bright-field images (Fig. 5c). Fig. 6a shows a high-resolution ADF-STEM image of the area used for the EELS analyses, with EELS spectra shown in Fig. 6b. EELS spectra of the calcite area showed the expected edges for carbon, calcium and oxygen, while the dark dots showed

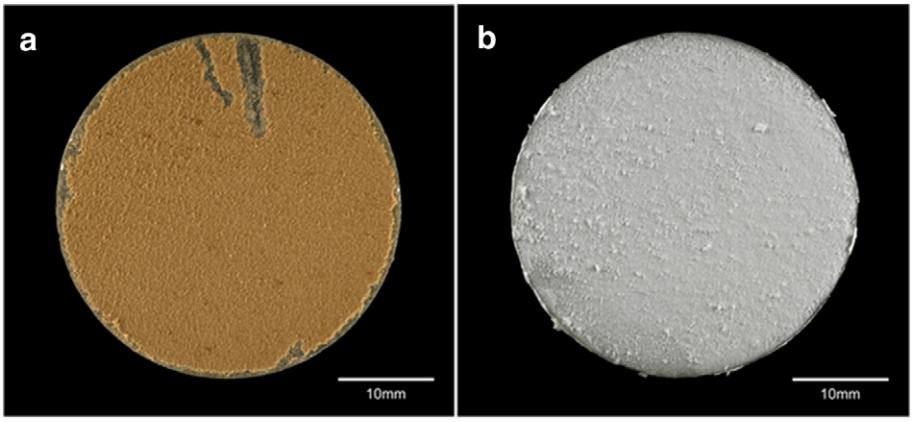

Fig. 4. Photographs of glass slides placed at the bottom of the microcosms showing (a) brown – orange coloured calcium carbonate precipitates formed in the presence of negatively charged NPs (l-negNPs in this example), and (b) white calcium carbonate precipitated in the absence of NPs. Scale bars both 10 mm.

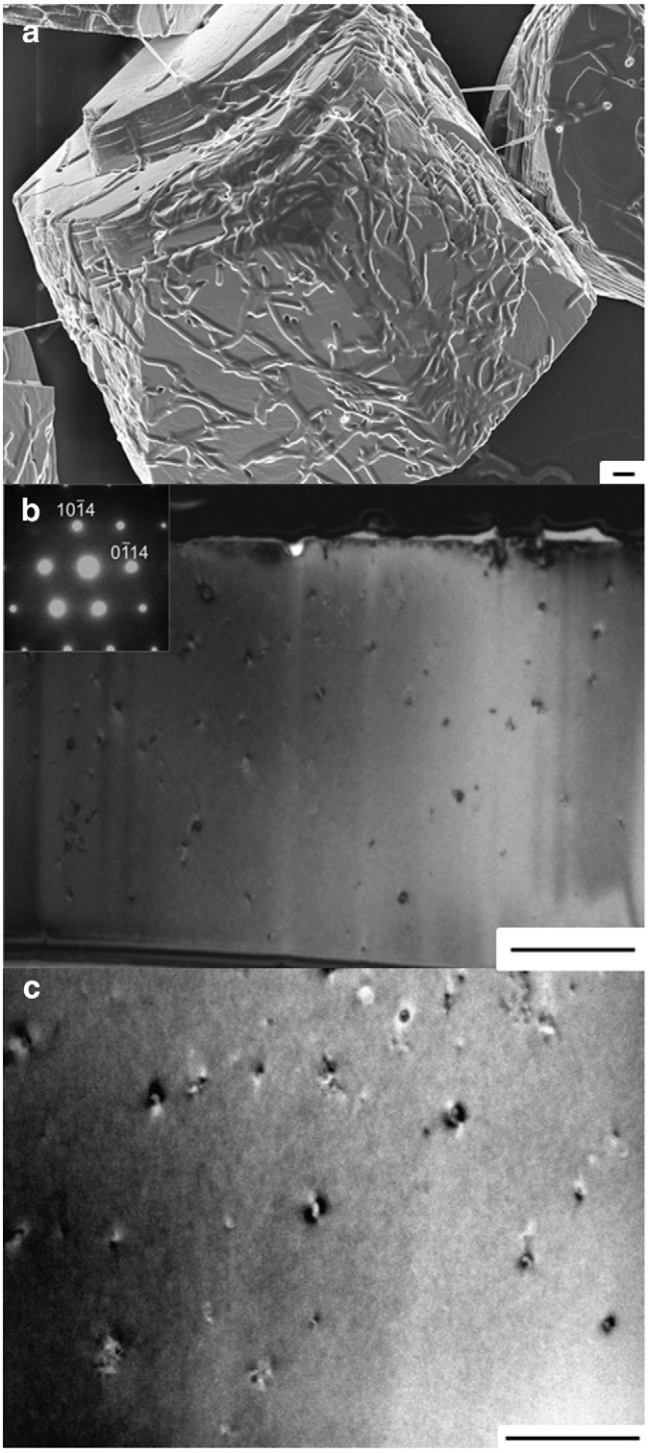

Fig. 5. a) SEM image illustrating typical rhombohedral calcite crystals precipitated in the presence of NPs with *S. pasteurii* attached to the crystal surfaces and embedded within (scale bar is 2 μm). b, c) Bright-field TEM images of foils milled (with FIB technique) from a calcite sample taken from the l-negNP experiment. Image (b) was obtained with the crystal oriented close to its [$\bar{4}$401] zone axis (indexed SAED pattern shown in inset). The black band along the top edge of the image is the platinum strap that was deposited on the {$10\bar{1}4$} parallel crystal surface prior to FIB milling, and the vertical streaks are ion milling artefacts (scale bar 1 μm). Under these imaging conditions the local elastic strain induced in the calcite crystal structure by the NP inclusions is highlighted by small areas of high contrast, giving the crystal a 'speckled' appearance (b), which is shown in higher magnification in (c) Scale bar 500 nm.

reduced levels of carbon and calcium, and a clear peak for iron, consistent with these being the iron-oxide core of the NPs. Quantitative chemical evaluation was not possible because the sample quickly decomposed under the high electron dose rates required for spectroscopy, even under fast acquisition (0.02 s per spectrum) and low accelerating voltage. This all demonstrates the nanoparticles are being effectively encapsulated inside the growing calcite crystals.

3.3. Thermodynamic and kinetic considerations

In this study, NPs with a negative surface charge (s-negNPs and l-negNPs) were successfully captured, while the immobilization of positively charged NPs (s-posNP) was less effective. Unlike solid-phase capture of dissolved ions such as Sr^{90}, NPs will not be incorporated into the crystal lattice by isomorphic replacement of calcium. Instead, NPs are occluded within the mineral as it forms, causing the mineral to grow around it, increasing overall strain on the crystal.

The large variations in capture efficiency between the positive and negative NPs might be best explained by electrostatic interactions controlling either nucleation, nanoparticle occlusion, or indeed both. The immobilization of negative NPs is extremely efficient, which could be due to rapid sorption of dissolved Ca^{2+} ions onto the negative NP surfaces, which then lowers the activation energy for $CaCO_3$ nucleation. If the negatively charged NPs are indeed acting as nucleation sites, the calculated critical saturation required for calcite nucleation, S_{crit}, should be lower for the s-negNPs and l-negNPs experiment compared to the s-posNPs. However, S_{crit} values are broadly similar for all tested NP types, particularly where the goodness of fit (R^2 values) is higher than 0.9 (Table 1). Thus, there is no clear evidence of NP type impacting S_{crit} under the experimental conditions used here. Instead, it is suggested here that due to the fairly high $CaCO_3$ saturation levels present in the experiments here, $CaCO_3$ nucleation was mainly homogenous (i.e., nucleation without a surface catalyst). Moreover, when looking at the calculated rate constants for calcite precipitation, these are also similar between the three tested NPs (for fits with $R^2 \geq 0.9$, Table 1), indicating that like nucleation, crystal growth was not majorly affected by the presence of NPs of different types. Again, calcite supersaturation was probably sufficiently high enough to drive precipitation at similar rates in all experiments.

When the relative rate of NP capture is compared to calcite precipitation rate, it is noted that negatively charged NPs are removed at a faster rate during the early stages of calcium carbonate precipitation, with ~50% of the s-negNPs captured during the first ~15% of calcite precipitation. (Fig. S1, Supplemental information). This may be explained by invoking a shift from homogeneous nucleation and fast growth, to growth on pre-existing surfaces. During the early stages, calcite nuclei are forming homogenously and consequently growing in suspension, thus capturing the NPs dispersed in solution. It is during this early stage of crystallization that most nanoparticles are being removed. However, during the later stages of the experiment, the saturation state with respect to calcite is greatly reduced (due to calcite precipitation) and thus precipitation may occur preferentially on pre-formed precipitates, i.e. those crystals that have already settled to the bottom of the reaction flask or adhered to its walls. Thus homogenous nucleation and growth in suspension is greatly reduced, leaving uncaptured NPs in solution. This then has implications for nanoparticle capture in natural settings. When the system is weakly supersaturated and nucleation is on mineral surfaces (e.g. the surfaces of a pore), nanoparticle capture will occur, but will likely be slower than if saturation states are higher and nucleation is occurring homogeneously (e.g. in the pore fluid). In the work shown here, a reinjection of calcium carbonate and urea drove further calcite precipitation to occur homogeneously in suspension (Fig. 3). Here, the stimulation of another homogeneous nucleation event resulted in 100% removal of l-negNPs through solid phase capture. This has implications for possible in-field application of this method for immobilization of nanoparticle contaminants. i.e. NP

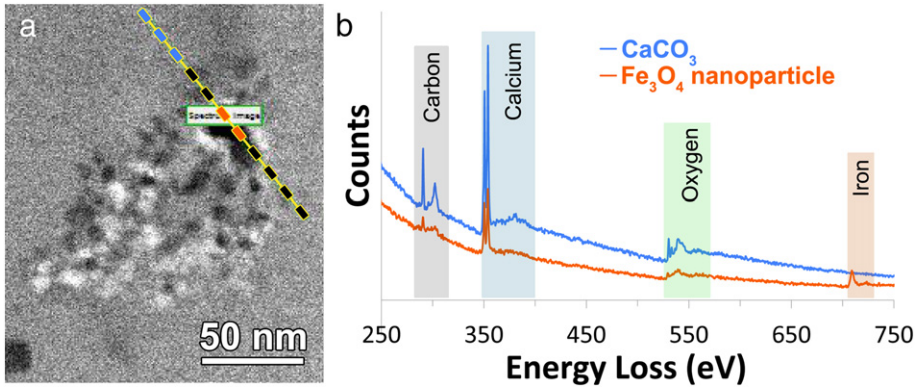

Fig. 6. (a) ADF-STEM image of a cluster of NPs (black dots) occluded in the calcite crystal. An EELS line scan was taken along the line indicated; (b) The upper, blue EELS spectrum, is the sum of EELS spectra collected in the calcite region (i.e., blue section of the line scan indicated in a) and the lower, orange EELS spectrum is the sum of EELS spectra collected in the NP region (i.e., orange section of the line scan indicated in a).

immobilization would be improved by multiple injections. For in-field remediation of NPs the extent of calcite precipitation will be, in part, depend on the availability of dissolved Ca^{2+} in the system. Groundwaters will have relatively low Ca^{2+} concentrations, but may have sufficient calcium for capture of pollutants. For example, the Eastern Snake River Plain Aquifer, Idaho, exhibits ~1.75 mM Ca^{2+}, and calcite precipitation and dissolved Sr^{2+} capture can be driven without further Ca^{2+} addition (Mitchell and Ferris, 2005). In this study we utilized a significantly higher concentration of 100 mM Ca^{2+} to capture NPs. These higher concentrations would require additional Ca^{2+} to be pumped into the aquifer. Whether much lower Ca^{2+} concentrations can lead to successful NP capture is worthy of further investigation.

3.4. Role of surface interaction in NP capture

Since $CaCO_3$ nucleation does not seem to be affected by the presence of negatively or positively charged NPs at the concentration used here, it is hypothesised that NP capture efficiency is determined by how well the NPs attach to the growing calcite surfaces, whereby strongly attached NPs get occluded by the growing solidification front. Previous studies have investigated incorporation of foreign particles using inorganically driven mineralisation and have shown that particle occlusion is dependent on the interactions between the particle and the advancing solidification front. For example, (Kim et al., 2010) investigated the occlusion of functionalised latex colloids (220–250 nm in diameter) during inorganically driven calcite precipitation and reported greater incorporation of particles with higher abundances of anionic surface groups. This agrees with what was observed here. At the pH range in this study, calcite exhibits a positive surface charge (Eriksson et al., 2007), thus the electrostatic attraction between the negatively charged NPs and the positively charged calcite surface seems to facilitate occlusion, while electrostatic repulsion between positively charged NPs and calcite inhibits occlusion.

Table 1
Summary of kinetic parameters for calcite precipitation: 1st order rate constant (k_p, in mM d^{-1}) and critical saturation state at which calcite precipitation occurred (S_{crit}).

NP	Replica	k_p (R^2 values)	S_{crit} (R^2 values)
s-negNP	1	0.11 (0.93)	2.02 (0.93)
	2	0.02 (0.66)	2.17 (0.66)
	3	0.09 (0.73)	2.21 (0.73)
s-posNP	1	–[a]	–[a]
	2	0.09 (0.96)	2.12 (0.96)
	3	0.04 (0.81)	2.25 (0.81)
l-negNP	1	0.12 (0.92)	2.11 (0.92)
	2	0.02 (0.55)	2.45 (0.55)
	3	–[a]	–[a]

[a] Parameter estimation failed.

Possible interaction scenarios between nanoparticles and the calcite surface were explored using DLVO and XDLVO theory (Fig. 7). DLVO calculations for calcite and small negative NPs indicates that interaction energies are attractive and attraction increases exponentially as the two surfaces approach each other (dashed line, Fig. 7). This is consistent with the efficient capture of small negative NPs by calcite seen experimentally, suggesting strong binding of NPs to the calcite surface facilitated occlusion. Conversely, DLVO interaction energies between calcite and the positively charged NPs show a small secondary energy minima at around 4 nm, and a repulsive energy barrier at around 2 nm (solid line Fig. 7). The energy barrier would hinder attachment to the calcite surface and any NPs sitting in the secondary energy minima would be more weakly bound. Again, this is consistent with the poorer capture of positively charged NPs by calcite. While DLVO results supported the experimental data, XDLVO did not appear to provide a suitable interaction scenario. The addition of Lewis acid-base properties overwhelmed any influence from van der Waals or electrostatic forces, resulting in a significant repulsive force for both negative and positive NPs (Fig. 7). Moreover, the XDLVO profiles were identical for both positive and negative nanoparticles and thus unable to discriminate any potential

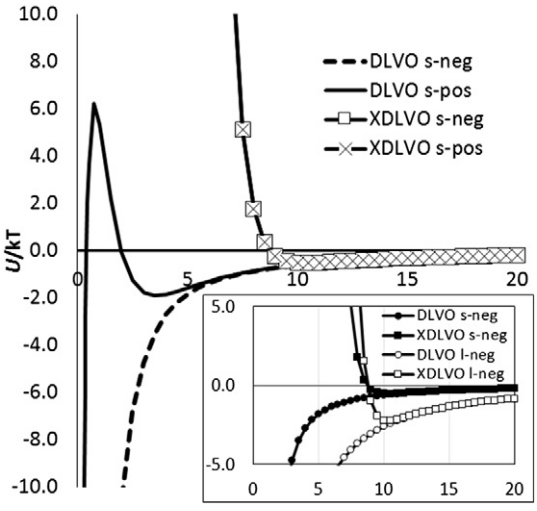

Fig. 7. Interaction energies between the nanoparticle and calcite surfaces for both DVLO and XDLVO models. Main figure compares small negative and small positively charged nanoparticles. Inset figure compares large and small nanoparticles. s-neg = small negative nanoparticle; s-pos = small positive nanoparticle; l-neg = large negative naparticle. Results are shown for total interaction energies normalized to kT (U/kT). Negative U/kT values are attractive, positive values are repulsive. DLVO = U_{DLVO}; XDLVO = U_{XDLVO} (see Eqs. (4) and (5)). In both graphs the x-axis is seperation distance in nm.

scenarios explaining the differences in capture efficiency. It is likely that Lewis acid-base properties for the dextran (calculated here from published parameters) were not representative of the particular dextran on the NP surface and thus experimental verification of the Lewis acid-base properties of these specific nanoparticles would be required. Interaction energies were also compared for both large and small negative NPs. DLVO model shows that attractive forces are greater for the larger NP compared to the small NP (Fig. 7 inset). Despite the slightly smaller zeta potential of the larger NP, its larger size has facilitated greater attraction to the calcite in the DVLO calculations. Moreover, the larger particle should also generate more viscous drag as it is pushed forward by the growing calcite particle, adding an additional attractive force facilitating uptake of the large NP (Kim et al., 2010). However, experimental results showed that slightly less large NPs were captured compared to small NPs (Fig. 1). Evidently, DLVO based interaction energies and viscous drag are not sufficient to explain the experimentally observed differences between occlusion of the large and small nanoparticle. It is speculated here that energy requirements for crystal growth around the larger NP, generating greater crystal distortion and strain, may reduce large NP occlusion. Occluding particles can generate strain which reduces the driving force for crystallization and cause difficulty in growing the mineral back over the occluded particle (Cho et al., 2016). The influence of the NP size on crystal growth may thus play a key role in controlling capture efficiency.

3.5. Further implications

The bacterium *Sporosarcina pasteurii* was used in this study as it is the commonly used model organism for ureolytic calcite precipitation investigations. However, it is notable that ureolytic capability is common in many groundwater and soil organisms, and thus there are a diverse range of organisms that can precipitate calcite via this pathway (Hammes et al., 2003). The capture of nanoparticles by ureolytic calcite precipitation is thus likely achievable by a diverse range of bacteria. Different species, however, can produce different rates of ureolysis and thus different rates of calcite precipitation. The impact this has on nanoparticle capture is worthy of further investigation. For example, slower growing calcite crystals might generate less viscous drag on the NP, possibly reducing capture efficiency. Interestingly, different bacteria have been shown to generate calcite precipitates with different morphologies (Hammes et al., 2003). However, whether these morphological differences might influence NP capture is unknown at this stage.

Microbially driven precipitation of calcite is common in the environment. While this study explored ureolytic calcite precipitation, there are numerous other pathways which can precipitate carbonates, including photosynthesis (Merz, 1992), denitrification (Martin et al., 2013), and fungal metabolic processes (Bindschedler et al., 2016). One would expect that calcite driven by these processes would also have the potential to immobilize NPs trough occlusion.

While this study has focused upon bacterially driven calcite precipitation, there are numerous other microbially driven mineral precipitation systems which have the potential for occlusion of NPs, such as the oxidation of Mn(II) (Sujith and Bharathi, 2011), Fe oxidation and reduction (Gault et al., 2012), or enzymatic precipitation of phosphate minerals (Schulz and Schulz, 2005). Critically, the variety of minerals that can be precipitated by bacteria display a range of surface charges (Glasauer et al., 2001; Gray et al., 1978; Harding et al., 2005) enabling them to interact with a wide variety of NP surface charges. Evidently there is significant potential for capture of nanoparticles by microbial mineral precipitation, whether naturally or through stimulated approaches for remediation of nanoparticulate pollutants.

The successful identification of nanoparticles trapped in calcite by TEM of FIB milled samples indicates such an approach could be used to explore nanoparticles trapped in calcite, or indeed any other mineral, from natural settings. Calcium carbonate precipitation is common in a diverse range of environments, including aquifers, diagenetic pore waters, hot springs and the marine environment (O'Reilly et al., 2017; Pentecost, 1995; Suzuki et al., 2016). Such systems may occlude nanoparticles (either manufactured or natural), and thus might record past natural processes or pollution events. Indeed, the FIB-TEM approach has recently recorded uranium nanoparticles embedded within calcite from a deep aquifer (Suzuki et al., 2016). Moreover, the calcite was proposed to have been microbially precipitated by anaerobic oxidation of organic matter. The implications of nanoparticle/mineral surface charge, DLVO energies and viscous drag explored in this study could be applied to explore nanoparticle entrapment mechanisms for this and other naturally occurring nanoparticle/mineral systems.

4. Conclusion

The results presented here demonstrate that microbially mediated calcite precipitation captured negatively charged NPs while positively charged NPs were captured much less successfully which facilitated occlusion. This was likely due to electrostatic attraction between the negative NP and positive calcite surface. This was supported by DLVO calculations which showed stronger attraction to the calcite by negative NPs, but weaker attraction by positive NPs. Analysis by TEM confirmed the NPs had been occluded inside the calcite minerals. k_p and S_{crit} values were broadly similar for all NP types tested suggesting NPs were not acting as significant nucleation sites for calcium carbonate and that NP type did not impact precipitation rate. Overall, these results illustrate the potential of biogenic mineral precipitation to capture NPs in natural systems

Acknowledgements

This work was undertaken with financial support from the Engineering and Physical Sciences Research Council, UK (grant number EP/G063699/1), and through an EPSRC funded PhD studentship.

Appendix A. Supplementary data

Supplementary data to this article can be found online at http://dx.doi.org/10.1016/j.chemgeo.2017.02.005.

References

Basnet, M., Di Tommaso, C., Ghoshal, S., Tufenkji, N., 2015. Reduced transport potential of a palladium-doped zero valent iron nanoparticle in a water saturated loamy sand. Water Res. 68, 354–363.
Bindschedler, S., Cailleau, G., Verrecchia, E., 2016. Role of fungi in the biomineralization of calcite. Minerals 6 (2).
Braissant, O., et al., 2007. Exopolymeric substances of sulfate-reducing bacteria: interactions with calcium at alkaline pH and implication for formation of carbonate minerals. Geobiology 5 (4), 401–411.
Brar, S.K., Verma, M., Tyagi, R.D., Surampalli, R.Y., 2010. Engineered nanoparticles in wastewater and wastewater sludge - evidence and impacts. Waste Manag. 30 (3), 504–520.
Caballero-Guzman, A., Nowack, B., 2016. A critical review of engineered nanomaterial release data: are current data useful for material flow modeling? Environ. Pollut. 213, 502–517.
Cho, K.R., et al., 2016. Direct observation of mineral-organic composite formation reveals occlusion mechanism. Nat. Commun. 7.
Dietrich, L.A.S., Sahu, M., Biswas, P., Fein, J.B., 2012. Experimental study of TiO2 nanoparticle adhesion to silica and Fe(III) oxide-coated silica surfaces. Chem. Geol. 332, 148–156.
Eriksson, R., Merta, J., Rosenholm, J.B., 2007. The calcite/water interface I. Surface charge in indifferent electrolyte media and the influence of low-molecular-weight polyelectrolyte. J. Colloid Interface Sci. 313 (1), 184–193.
Feriancikova, L., Xu, S.P., 2012. Deposition and remobilization of graphene oxide within saturated sand packs. J. Hazard. Mater. 235, 194–200.
Ferris, F.G., Phoenix, V., Fujita, Y., Smith, R.W., 2004. Kinetics of calcite precipitation induced by ureolytic bacteria at 10 to 20 degrees C in artificial groundwater. Geochim. Cosmochim. Acta 68 (8), 1701–1710.
Fujita, Y., Taylor, J.L., Wendt, L.M., Reed, D.W., Smith, R.W., 2010. Evaluating the potential of native ureolytic microbes to remediate a Sr-90 contaminated environment. Environ. Sci. Technol. 44 (19), 7652–7658.
Gault, A.G., et al., 2012. Seasonal changes in mineralogy, geochemistry and microbial community of bacteriogenic iron oxides (BIOS) deposited in a circumneutral wetland. Geomicrobiol J. 29 (2), 161–172.

Glasauer, S., Langley, S., Beveridge, T.J., 2001. Sorption of Fe (hydr)oxides to the surface of Shewanella putrefaciens: cell-bound fine-grained minerals are not always formed de novo. Appl. Environ. Microbiol. 67 (12), 5544–5550.
Gray, M.J., Malati, M.A., Rophael, M.W., 1978. The point of zero charge of manganese dioxides. J. Electroanal. Chem. Interfacial Electrochem. 89, 135–140.
Hammes, F., Boon, N., de Villiers, J., Verstraete, W., Siciliano, S.D., 2003. Strain-specific ureolytic microbial calcium carbonate precipitation. Appl. Environ. Microbiol. 69 (8), 4901–4909.
Handley-Sidhu, S., Renshaw, J.C., Yong, P., Kerley, R., Macaskie, L.E., 2011. Nano-crystalline hydroxyapatite bio-mineral for the treatment of strontium from aqueous solutions. Biotechnol. Lett. 33 (1), 79–87.
Harding, I.S., Rashid, N., Hing, K.A., 2005. Surface charge and the effect of excess calcium ions on the hydroxyapatite surface. Biomaterials 26 (34), 6818–6826.
Hoek, E.M.V., Agarwal, G.K., 2006. Extended DLVO interactions between spherical particles and rough surfaces. J. Colloid Interface Sci. 298 (1), 50–58.
Hofmann, T., von der Kammer, F., 2009. Estimating the relevance of engineered carbonaceous nanoparticle facilitated transport of hydrophobic organic contaminants in porous media. Environ. Pollut. 157 (4), 1117–1126.
Hong, Y.S., Honda, R.J., Myung, N.V., Walker, S.L., 2009. Transport of iron-based nanoparticles: role of magnetic properties. Environ. Sci. Technol. 43 (23), 8834–8839.
Kim, Y.Y., et al., 2010. Bio-inspired synthesis and mechanical properties of calcite-polymer particle composites. Adv. Mater. 22 (18) (2082-+).
Kim, Y.Y., et al., 2016. Structure and properties of nanocomposites formed by the occlusion of block copolymer worms and vesicles within calcite crystals. Adv. Funct. Mater. 26 (9), 1382–1392.
Levard, C., Hotze, E.M., Lowry, G.V., Brown, G.E., 2012. Environmental transformations of silver nanoparticles: impact on stability and toxicity. Environ. Sci. Technol. 46 (13), 6900–6914.
Limbach, L.K., et al., 2008. Removal of oxide nanoparticles in a model wastewater treatment plant: influence of agglomeration and surfactants on clearing efficiency. Environ. Sci. Technol. 42 (15), 5828–5833.
Martin, D., Dodds, K., Butler, I.B., Ngwenya, B.T., 2013. Carbonate precipitation under pressure for bioengineering in the anaerobic subsurface via denitrification. Environ. Sci. Technol. 47 (15), 8692–8699.
Martinez, R.E., Pedersen, K., Ferris, F.G., 2004. Cadmium complexation by bacteriogenic iron oxides from a subterranean environment. J. Colloid Interface Sci. 275 (1), 82–89.
Merz, M.U.E., 1992. The biology of carbonate precipitation by cyanobacteria. Facies 26 (81-11).
Mitchell, A.C., Ferris, F.G., 2005. The coprecipitation of Sr into calcite precipitates induced by bacterial ureolysis in artificial groundwater: temperature and kinetic dependence. Geochim. Cosmochim. Acta 69 (17), 4199–4210.
O'Reilly, S.S., et al., 2017. Molecular biosignatures reveal common benthic microbial sources of organic matter in ooids and grapestones from Pigeon Cay, The Bahamas. Geobiology 15 (1), 112–130.
Pei, Y.J., Chen, X., Xiong, D.D., Liao, S.J., Wang, G.J., 2013. Removal and recovery of toxic silver ion using deep-sea bacterial generated biogenic manganese oxides. PLoS One 8 (12).
Pentecost, A., 1995. The microbial ecology of some Italian hot-spring travertines. Microbios 81 (326), 45–58.
Schulz, H.N., Schulz, H.D., 2005. Large sulfur bacteria and the formation of phosphorite. Science 307 (5708), 416–418.
Sujith, P.P., Bharathi, P.A., 2011. Manganese oxidation by bacteria: biogeochemical aspects. Prog. Mol. Subcell. Biol. 52 (49-76 pp).
Suzuki, Y., et al., 2016. Formation and geological sequestration of uranium nanoparticles in deep granitic aquifer. Sci. Rep. 6.
Tobler, D.J., et al., 2011. Comparison of rates of ureolysis between *Sporosarcina pasteurii* and an indigenous groundwater community under conditions required to precipitate large volumes of calcite. Geochim. Cosmochim. Acta 75 (11), 3290–3301.
van Paassen, L.A., et al., 2010. Potential soil reinforcement by biological denitrification. Ecol. Eng. 36 (2), 168–175.
Warren, L.A., Maurice, P.A., Parmar, N., Ferris, F.G., 2001. Microbially mediated calcium carbonate precipitation: implications for interpreting calcite precipitation and for solid-phase capture of inorganic contaminants. Geomicrobiol J. 18 (1), 93–115.
Yee, N., Fowle, D.A., Ferris, F.G., 2004. A Donnan potential model for metal sorption onto *Bacillus subtilis*. Geochim. Cosmochim. Acta 68 (18), 3657–3664.